Mon. Not. R. Astron. Soc. **270,** 580–596 (1994)

Multifrequency monitoring of the Seyfert 1 galaxy NGC 4593 – I. Isolating the nuclear emission

M. Santos-Lleó,[1,2] J. Clavel,[3] P. Barr,[3] I. S. Glass,[4] D. Pelat,[1] B. M. Peterson[5] and G. Reichert[6]

[1] *Observatoire de Paris, DAEC 92195 Meudon Cedex, France*
[2] *ESA IUE Observatory, PO Box 50727, 28080 Madrid, Spain*
[3] *ISO Observatory, Code SAI, ESTEC, Postbus 299, 2200 AG Noordwijk, The Netherlands*
[4] *South African Astronomical Observatory, PO Box 9, Observatory 7935, Cape, South Africa*
[5] *Department of Astronomy, Ohio State University, 174 W. 18th Avenue, Columbus, OH 43210, USA*
[6] *NASA-Goddard Space Flight Center, Code 684.9, Building 21, Greenbelt, MD 20771, USA*

Accepted 1994 May 3. Received 1994 April 28; in original form 1994 January 20

ABSTRACT

We present data obtained within a campaign to monitor spectral variations in the low-luminosity Seyfert 1 galaxy NGC 4593, at X-ray, ultraviolet, optical and near-IR (*J*, *H*, *K* and *L*) frequencies. The different 'parasitic' contributions that contaminate the pure nuclear continuous emission have been isolated and modelled. The light from the composite stellar population and the dust in the bulge and disc of the underlying galaxy are characterized by a spectral energy distribution similar to that of the Sb spiral M31. Its surface brightness profile is modelled with two components and provides the luminosity through any given aperture. Stars are responsible for as much as 70–85 per cent of the 5600-Å flux through a 4×4 arcsec^2 square aperture. The 'small bump' which characterizes the spectral energy distribution of active nuclei in the 2000–4000 Å range is well accounted for by many blended broad Fe II lines plus Balmer continuum emission. On average ~64 per cent of the total 2710-Å flux is due to Fe II plus Balmer emission. Almost half of the broad-line cooling is due to Fe II line emission. The pattern of variability of the pure nuclear continuum, as well as the broad lines and their implications, is discussed in an accompanying paper.

Key words: galaxies: individual: NGC 4593 – galaxies: nuclei – galaxies: Seyfert – infrared: galaxies – ultraviolet: galaxies – X-rays: galaxies.

1 INTRODUCTION

Active galactic nuclei (AGNs) are powerful emitters, from radio to γ-ray frequencies, with approximately the same power radiated per frequency decade. The origin of their spectral energy distribution (SED) is still poorly understood. For instance, one of its salient features, the so-called 'big bump' (which in a log (flux) versus log (frequency) diagram shows up as an excess of energy over the $\lambda \simeq 1$ μm to $\lambda \leq 1000$ Å wavelength range; e.g. Sanders et al. 1989) is extensively claimed to originate in a thin accretion disc (Lynden-Bell 1969). Many problems, however, plague this model (Clavel et al. 1992 and references therein). In order to draw a consistent picture of the origin of the whole AGN electromagnetic spectrum, the knowledge of its SED in the largest possible range is needed. In particular, to constrain the accretion disc model, we require fluxes from at least the extreme UV to the optical or near-infrared. The variability of the nuclear source, the rich emission-line spectrum and the relationship between continuum and line variations have all been successfuly used to probe the nature of the source. Many difficulties arise, however, when connecting data from these spectral windows. The difficulties are primarily due to the different instrument configurations, which give rise to different relative contributions from sources other than the pure continuous AGN emission. The main such 'parasitic' contributions are (i) cool interstellar dust emission from the underlying galactic disc in the medium and far-IR; (ii) stellar emission in the optical and near-IR; (iii) Balmer continuum and low-contrast Fe II line emission in the optical and near-ultraviolet.

In low-luminosity AGN, stellar and dust emission can provide a significant fraction of the total observed light. In addition, the underlying galaxy surface brightness distribution is fairly extended, in contrast to the point-like AGN. Therefore their relative contributions depend on both spec-

trograph aperture and seeing. Hence only the knowledge of the stellar luminosity profile would allow comparison of data obtained with different instruments and observing conditions.

The emission of many (thousands) Fe II lines and of the Balmer continuum produce a pseudo-continuum in the spectral region of ~2000–4000 Å, usually referred to as the 'small bump'. Fe II emission is often important in the optical range as well. There are many difficulties, both observational and intrinsic, that complicate the measurement of these features (see Maoz et al. 1993 or Wills, Netzer & Wills 1985 for a discussion). Nevertheless, Fe II and Balmer emission are important, not only to allow determination of the true shape of the nuclear continuous radiation, but also because they contribute a large fraction of the total emission-line cooling in the broad-line region (BLR). For instance, in NGC 5548 the 'small bump' is estimated to represent 30–40 per cent of the total flux at 2700 Å (Wamsteker et al. 1990; Clavel et al. 1991) and 1/3 of the line flux (Maoz et al. 1993). In NGC 3783 it is responsible for the dilution of the far-UV, making it difficult to estimate the real shape and variability of the UV continuum (Reichert et al. 1994). Moreover, not only the continuum but also other broad emission lines are contaminated by the Fe II emission, the most important being Hβ and the [O III] $\lambda\lambda$4959, 5007 doublet in the optical and Mg II λ2798 in the UV. As an example, Reichert et al. (1994) argue that about 30–50 per cent of the measured Mg II flux in NGC 3783 can be made up of Fe II if the latter is not properly taken into account.

In this paper, we report the results of a multiwavelength monitoring programme of a Seyfert 1, NGC 4593, from the near-IR to X-rays. Here we concentrate on the description of the observations and the analysis of the data. The 'parasitic' contributions already mentioned are modelled to allow measurements of their intensities and subtraction of their contributions. An accompanying paper (Santos-Lleó et al. 1994, hereafter Paper 2) discusses the pure nuclear energy distribution, its pattern of variability and that of the broad emission lines and their implications.

NGC 4593 is a bright close-by ($z = 0.0083$) barred spiral galaxy with a Seyfert 1 type nucleus (Lewis, McAlpine & Koski 1978; McAlpine, Williams & Lewis 1979). It contains a weak (6.6×10^{20} W Hz^{-1} at 20 cm, $H_0 = 75$ km s^{-1} Mpc^{-1} used throughout this paper), compact (< 37 pc), flat-spectrum ($\alpha = -0.23$) radio source (Ulvestad & Wilson 1984). Its broad-band infrared spectrum was measured up to 100 μm by the *IRAS* satellite (*IRAS* Point Source Catalog 1985). Lawrence et al. (1991) give an upper limit of 97 mJy at 1.082 mm, which implies that the spectrum must rise sharply ($\alpha \sim +2$) from the 1-mm to the far-IR range. The near-infrared *JHKL* spectrum of NGC 4593 is similar to that of other Seyfert 1 galaxies (Glass & Moorwood 1985). NGC 4593 is variable, both in the continuum and in the emission lines, at UV (Clavel et al. 1983), optical (Peterson, Crenshaw & Meyers 1985) and X-ray energies (Dower et al. 1980). Clavel (1983) also reported a rapid (≤ 3 d) two-folding time of its far-UV continuum flux. With $L_{2-10\ \mathrm{keV}} = 1.1 \times 10^{43}$ erg s^{-1}, NGC 4593 qualifies as a low-luminosity X-ray Seyfert 1. It has a nearly 'canonical' spectral index, $\alpha = 0.76^{+0.19}_{-0.09}$, and shows an excess of energy below approximately 1 keV (Turner & Pounds 1989). Its optical spectrum is weakly polarized, with a degree of linear polarization of 0.52 per cent (Martin et al. 1983) and 0.71 ± 0.35 per cent in the blue (Brindle et al. 1990), some of which could be intrinsic to NGC 4593, given the very low column density of interstellar material on the line of sight (2×10^{20} cm^{-2}; Elvis, Lockman & Wilkes 1989). Clavel et al. (1983) proposed a detailed model of the BLR in NGC 4593, where the high- and low-ionization lines arise from different regions.

2 OBSERVATIONS AND DATA ANALYSIS

Repeated observations of the nucleus of NGC 4593 have been performed at X-ray, ultraviolet, optical and near-IR wavelengths.

2.1 X-ray (*EXOSAT*)

Eight X-ray observations were carried out with *EXOSAT* between 1984 and 1986. The details are given in Table 1. Both low-energy (LE, from 0.05 to 2.0 keV; De Korte et al. 1981) and medium-energy (ME, from 0.7 to 50 keV; Turner, Smith & Zimmermann 1981) data are available from the satellite. In the LE, broad-band spectrophotometry is performed using different filters. The ME is typically operated with one half of the array pointed on-source and the other half pointed at an adjacent source-free region of the sky, in order to monitor the particle background. For a relatively weak source such as NGC 4593, the ME only yields usable data up to 10 keV. The ME background in each observation was determined using the difference spectra technique described by Parmar & Izzo (1986), except for the 1984 (Feb 3) observation when no array swaps were performed; in this case the background was measured during the slew off the source. In addition, during the 1984 February 3 observation, solar flaring activity seriously corrupted the data from detectors E and F (which lay on the side of the spacecraft closest to the sun vector); therefore only the data from detector H were used, and then only from intervals when no solar activity was evident in the other detectors.

A glance at Table 1 shows that both the soft and hard X-ray flux of NGC 4593 varied from observation to observation. In addition, during five out of seven observations, significant variability took place *during* the observation. These rapid variations of the X-ray flux have been analysed by Barr et al. (1987). They find that, on one occasion, the ME flux doubled in 1.1 h, with a trend for the characteristic timescale Δt to increase, together with the average luminosity L_X of NGC 4593, during the observation. Such a trend is reminiscent of the $\Delta t/L_X$ correlation found in a sample of AGNs by Barr & Mushotzky (1986). Here, we concentrate on the long-term (> 1 d) variations of the *mean* X-ray flux, averaged over the course of an observation. It is worth stressing that the amplitude of these slow variations is significantly larger (by a factor of 2–10) than that of the rapid fluctuations.

For each observation, a number of power-law spectral models were folded through the detectors' responses and fitted simultaneously to the ME and LE data. The results are shown in Table 2; errors are 68 per cent confidence (cf. Avni 1976). For those observations when rapid X-ray variability was occurring and when different LE filters were used, only data taken simultaneously with both detectors were fitted. The results from each filter combination are shown separately in the table (e.g. 1984 July 1, 1985 June 25 and July 4).

Table 1. *EXOSAT* observations of NGC 4593.

Date		Start	Exp.T.	ME(2-6keV)	LE Lexan	LE Al–P	LE Boron
day mon yr	JD[a]	UT	Min.	cts/s/(750cm^2)		counts s^{-1}	
3 Feb 84	5735.4	22.01	160	2.20±0.20	0.123±0.008	0.081±0.006	···
2 Jun 84	5853.8	06.30	360	2.21±0.05	0.192±0.009	0.086±0.007	0.014±0.002
1 Jul 84	5882.5	00.55	400	2.71±0.03	0.19±0.017	0.082±0.005	0.0125±0.0027
25 Jun 85	6241.8	06:00	630	0.85±0.02	0.036±0.002	0.018±0.0014	···
29 Jun 85	6246.2	17:25	340	0.92±0.06	0.051±0.003	0.0195±0.003	···
4 Jul 85	6251.2	15:40	670	1.10±0.02	0.051±0.003	0.0227±0.0016	···
9 Jan 86	6440.5	23:15	1680	2.15±0.02	0.188±0.006	···	···
5 Feb 86	6467.4	21:15	750	···	0.207±0.003	···	···

[a]JD 244 0000.

Table 2. Power-law[a] fits to the X-ray spectra.

JD	n_o	Photon index,Γ	N_H	χ^2/dof	χ^2/dof
-2,440,000	10^{-3}		10^{20} atoms cm^{-2}		N_H=1.97x10^{20}
5735.4	15.0±2.0	2.1±0.2	$3.7^{+2.4}_{-1.4}$	5.3/24	9.1/25
5853.8	11.1±0.6	1.87±0.06	1.0±0.3	39.1/30	58.5/31
5882.5[b]	12.0±1	1.65±0.09	$0.78^{+0.41}_{-0.31}$	20.4/26	33.1/27
5882.5[c]	12.2±0.8	1.75±0.08	$0.93^{+0.7}_{-0.5}$	20.0/25	24.7/26
5882.5[d]	11.8±1	1.8±0.1	$12.8^{+21.5}_{-8}$	28.7/25	31.0/26
6241.8[e]	3.25±0.25	1.67±0.1	1.4±0.5	40.8/25	43.0/26
6246.2	$3.4^{+0.8}_{-0.5}$	1.6±0.3	$0.8^{+1.2}_{-0.7}$	26.6/30	28.9/31
6251.2	3.8±0.3	1.59±0.08	$0.87^{+0.84}_{-0.54}$	16.9/25	26.1/26
6440.5	8.8±0.3	1.71±0.04	0.53±0.11	35.3/24	181.6/25

[a] $I(\varepsilon)\mathrm{d}\varepsilon = n_0\varepsilon^{-\Gamma}\mathrm{e}^{-\sigma N_H}\mathrm{d}\varepsilon$ photon cm^{-2} s^{-1} keV^{-1}.
[b]Interval when Lexan filter was used.
[c]Only Al-P filter used.
[d]Only Boron filter used.
[e]LE count rates adjusted to a 'mean' level so they are sampled as evenly as the ME.

For X-ray sources with equivalent hydrogen column density $\leq 10^{21}$ cm^{-2}, the spectral index is determined solely by the ME data and the column density by the LE data. The column density due to the interstellar medium in our galaxy in the line of sight to NGC 4593 has been measured directly by Elvis et al. (1989) to be $1.97 \pm 0.1 \times 10^{20}$; this represents a *lower* limit to the total column, since the absorption intrinsic to NGC 4593 may be non-zero. In Table 2 we also give the χ^2 values for power-law fits to the data with N_H fixed at 1.97×10^{20} atom cm^{-2}. During four observations – JD 244 0000: 5853, 5882, 6251, 6440 – the derived column densities from our X-ray data are significantly *lower* than this value (application of the F-test indicates this at $\geq$99.9 per cent confidence level). This is also true for the sample *as a whole*, from summing the χ^2 values for all observations; in other words, there is an excess soft X-ray flux over that predicted by a simple power-law model. This is the case even if the column intrinsic to NGC 4593 is zero, and so rules out partial covering or warm absorber models as the origin for the excess; the latter must be due to an intrinsic turn-up of the continuum. Such behaviour is quite common in Seyfert 1 galaxies (cf. Turner & Pounds 1989) and may be present in as many as 50 per cent of all systems.

We have tried to determine the strength of the soft excess in each filter by extrapolating a power law with spectral index derived from the ME data alone, and with N_H fixed at the local ISM value of 1.97×10^{20} cm^{-2}. This yields the predicted count rate in each filter, and the excess is simply the observed minus predicted count rate. The results are shown in Table 3(a). The quoted errors are 68 per cent confidence levels and include contributions due to the uncertainties in the observed LE count rate, the ME spectral index, and the Elvis et al. value of N_H (2×10^{20} atom cm^{-2}). We note that, if there is any absorption intrinsic to NGC 4593, the quoted soft excesses are too low. If, however, such intrinsic absorption is not variable in time, all excesses would be low by the same factor.

In addition, we have taken the data from the long (28 h) observation on 1986 January 9–11, when the source was undergoing rapid variability, and extracted spectra and LE count rates for the intervals when the source was in a 'high state' (ME flux above the mean) and 'low' state (below the mean), in order to search for *rapid* variations in the soft excess (Table 3b). Unfortunately this result is inconclusive; a variance analysis suggests variability in the soft excess within this observation at the 97.5 per cent confidence level only. The shortest time for which we have firm evidence of variability in the soft excess is the 119-d interval between 1984 February 3 and June 2 (JD: 5735 and 5854).

The excess is really present only in the Lexan filter, which both gives the highest signal-to-noise ratio and has the softest spectral response for extragalactic sources (the interstellar medium effectively blocks all X-rays with energy $\leq$100 eV so the window below 75 eV in the Al-P filter is not relevant

Table 3. (a) The soft excess count rate in NGC 4593.

JD	Γ, ME	LE Filter	Observed LE counts s^{-1}	Predicted counts s^{-1}	Soft excess counts s^{-1}	%
5735.4	$2.2^{+0.7}_{-0.6}$	Lexan	0.123	0.134±0.054	−0.011±0.03	0
5735.4		Al-P	0.081	0.07 ±0.037	0.01±0.03	13
5853.8	1.85±0.05	Lexan	0.192	0.122±0.006	0.07±0.01	36
5853.8		Al-P	0.086	0.0641±0.003	0.022±0.008	25
5882.5	1.65±0.1	Lexan	0.19	0.105±0.01	0.085±0.0197	45
5882.5	1.75±0.1	Al-P	0.082	0.0575±0.005	0.025±0.007	30
6241.8	1.67±0.1	Lexan	0.036	0.0276±0.009	0.008±0.009	23
6241.8	1.8±0.3	Al-P	0.0178	0.0155±0.0017	0.0023±0.0022	13
6246.2	1.65±0.3	Lexan	0.051	0.034±0.01	0.017±0.011	33
6246.2		Al-P	0.0195	0.0165±0.005	0.003±0.006	15
6251.2	1.59±0.1	Lexan	0.051	0.0323±0.0026	0.0187±0.004	37
6251.2		Al-P	0.0227	0.0183±0.0008	0.0043±0.016	19
6440.5	1.71±0.04	Lexan	0.188	0.087±0.008	0.1±0.01	54

(b) 'High' and 'low' state intervals on 1986 days 9 to 11.

	Γ, ME	ME counts s^{-1}	Observed LE counts s^{-1}	Predicted counts s^{-1}	Soft excess counts s^{-1}
"High state"	1.76±0.05	2.33±0.06	0.215±0.003	0.0911±0.01	0.124±0.011
"Low state"	1.74±0.05	1.74±0.03	0.149±0.003	0.067±0.017	0.082±0.018

here). The only difference between the spectral response of the Lexan and Al-P filters occurs below the carbon edge (240 eV); the fact that the excess is seen in Lexan but not Al-P indicates that most of the excess X-ray continuum probably arises *below* the carbon edge.

With only broad-band filter measurements available below 700 eV, it is not possible to discriminate between *different* spectral models for the shape of the soft excess. However, due to the lack of any discernible excess in the Al-P and Boron filters and in the lowest channels of the ME spectra, we can only set crude limits on the spectral properties of the excess for various individual models. In Table 4 we show the results of simultaneous fits to the ME and LE data, assuming a hard X-ray power with N_H fixed at 1.97×10^{20} and spectral index fixed at the ME best-fitting value, with various models for the soft excess.

To summarize, the X-rays are well fitted by a power law whose spectral index $\alpha=-0.75\pm0.05$ is constant and close to the average values for AGNs (Turner & Pounds 1989). The inferred hydrogen column density in the line of sight is significantly smaller than that measured at 21 cm (Elvis et al. 1989), therefore implying the existence of a soft X-ray excess in NGC 4593. In Table 5, we list the integrated X-ray flux from 2 to 10 keV, including published measurements from previous experiments.

2.2 Ultraviolet (*IUE*)

Ultraviolet (1200–3200 Å) low-resolution (1000 km s^{-1}) spectra were obtained with the *IUE* satellite (Boggess et al. 1978a, b) at 21 epochs, from 1979 to 1987. The observing procedure was standard, the Fine Error Sensor (FES) being used to acquire the nucleus and centre it into the spectrograph aperture. In all cases, the data were obtained through the larger aperture (10×20 arcsec^2). The first 16 epochs consisted of 8 h of observations, during which one short-wavelength (SWP; 1200–1950 Å) spectrum and one long-wavelength (LWP/R; 1900–3200 Å) spectrum were obtained. In 1987 June 24 and December 14, the observations lasted for 16 h, and five consecutive SWP spectra were obtained. Two LWP spectra could also be secured during the December shift by stacking series of 30-min exposures. For the remaining three epochs, only one SWP observation, of about 4-h duration, was performed. The exposure times are such that the signal is close to, but below, the saturation limit at the peak of the Lyα λ1216 and Mg II λ2798 emission lines in the SW and LW ranges, respectively. A couple of pixels turned out to be saturated in the Mg II line in 1981 May 7 and in 1985 February 11 and 15. Such a small amount of saturation has no significant impact on the measured flux. The observing dates, image sequential numbers and exposure times are listed in Table 6.

All the spectra have been processed or reprocessed with the latest version of the *IUE* low-resolution data reduction software (Bohlin, Holm & Lindler 1981). Obvious blemishes were manually removed from the 2D line-by-line spectrum before data extraction. We have corrected the LWR spectra for the loss of sensitivity of the LWR detector (Clavel, Gilmozzi & Prieto 1988). The amount of degradation of the SWP and LWP data was deemed too small to be worth compensating for (Bohlin & Grillmair 1987; Sonneborn & Garhart 1986).

From the 21-cm hydrogen column measurements of Elvis et al. (1989), and assuming a normal gas-to-dust ratio (Bohlin, Savage & Drake 1978), the amount of galactic reddening toward NGC 4593 is $E(B-V)=0.029$. This value of the colour excess, together with the extinction law of Seaton (1979), have been used to 'deredden' all the ultraviolet and optical spectra of NGC 4593.

Three representative UV spectra are displayed in Fig. 1, where it is obvious that both the continuum and the emission

Table 4. Restrictions to spectral models for the soft excess.

Spectral model	Relevant parameter	68% confidence limit
Power law	Photon spectral index	≥ 3.6
Blackbody	Temperature	$\leq 10^6$K
Optically thin thermal plasma (Mewe & Gronenschild)	Temperature	$\leq 10^6$K
Power law with exponential cutoff	ϵ-folding energy	$\leq$ 300eV

Table 5. X-ray flux history of NGC 4593.

Date (ddmmyy)	Instrument	$F_{2-10keV}$ (10^{-11} erg cm^{-2} s^{-1})
1971-73	Uhuru[a]	4.9±1.4
27Dec75	Ariel V[b]	3.4±0.3
02Jun78	HEAO1/A2[c]	3.6±0.7
04Jul78	HEAO1/MC[d]	1.0±0.4
25Jun79	HEAO2/SSS[e]	1.1±0.2
03Feb84	EXOSAT	2.2±0.5
02May84	EXOSAT	3.5±0.1
02Jul84	EXOSAT	4.6±0.3
25Jun85	EXOSAT	1.4±0.1
29Jun85	EXOSAT	1.6±0.5
05Jul85	EXOSAT	1.8±0.1
09Jan86	EXOSAT	3.5±0.1

[a]Forman et al. 1978.
[b]Bell-Burnell and Chiappetti 1984.
[c]Marshall et al. 1979.
[d]Dower et al. 1980.
[e]Reichert et al. 1985.

lines underwent significant variations. The mean continuum fluxes in suitable spectral 'windows' apparently devoid of emission lines are listed in Table 7. The selection of these intervals has been discussed by Clavel et al. (1983). There are no variations either of the emission line intensities or of the UV continuum flux in NGC 4593 on time-scales of 16 h or less (Paper 2). Therefore, for the two epochs (1987 June 24 and 1987 December 14), when five SWP spectra are available, the fluxes reported in Table 7 are averages over the values from the five individual spectra. The two standard deviations about both averages were also averaged and the result was taken to represent the error on the continuum flux shortward of 1950 Å for all epochs. This procedure is similar to that followed by Clavel et al. (1991) in the case of NGC 5548. For 1987 June 24 and December 14, we used the error on the mean. Another exception was SWP7508 for which, the continuum being barely above the detection threshold in most windows, the errors were arbitrarily multiplied by two. Longward of 1950 Å, the errors quoted are standard deviations from the mean flux in each continuum 'window'.

The fluxes of the four strongest emission lines, Lyα λ1216, C IV λ1549, C III] λ1909 and Mg II λ2798, at each epoch are listed in Table 8. This table also lists the Fe II UV data as modelled in Section 4. The line intensities have been measured by summing all the flux above the continuum in the intervals listed in the second row of the table. The Si IV λ1394, N IV] λ1486 lines and the He II λ1640 + O III] λ1663 blend are too weak to be reliably measured in most of the individual spectra. Only the flux to the red of the line peak was measured in the case of Lyα λ1216, since its blue wing is blended with the geocoronal feature. Assuming a symmetrical profile, the flux was further multiplied by two to account for the missing blue wing. The Lyα λ1216 flux contains a small contribution from the much weaker N V λ1240 line, enhanced when doubling the flux in the red half of Lyα. We estimate this contribution to be 15 per cent in the average. The continuum underlying each line was obtained by linearly interpolating the flux in the two windows immediately ajdacent to it. There are two exceptions: in the case of Lyα λ1216, the continuum intensity was assumed to be wavelength-independent and equal to the flux in the 1333-Å window, while, for the C III] λ1909 line, the continuum was obtained from a linear extrapolation of the 1726-Å and 1803-Å fluxes. As for the continuum (see previous paragraph), the errors on the line flux in the SWP range were derived from the standard deviation of the individual measurements on 1987 June 25 and 1987 December 14, except for these two epochs (where the error on the mean was used instead). The error on the Mg II λ2798 line intensity was assumed to be the same as that of C IV λ1549 scaled by the mean ratio of the square root of the number of raw counts in the spectrum. The errors were arbitrarily multiplied by two in the case of SWP7508 and LWR9818, to account for the relatively short exposure times.

We have measured separately the flux in the 'core' and that in the 'red wing' of Lyα λ1216 and C IV λ1549, at each epoch. In addition, and in order to compare the profiles of different lines, we have, when possible, performed Gaussian decomposition. The results are shown in Appendix A.

2.3 Optical

2.3.1 IUE *FES photometry*

Table 6 lists the broad-band optical flux of NGC 4593, as measured by the *IUE* FES S-20 photocathode in an equivalent 12-arcsec square aperture at an effective wavelength of 5200 Å. One FES measurement is automatically recorded before each ultraviolet exposure, which means that there are at least two (up to seven in 1987 June) measurements available at each epoch. The only exceptions are 1985 July 4 and

Table 6. Log of *IUE* observations.

Start Date (UT) (yr mon day)	JD-2,440,000	SWP Image N°	Exp. Time (min:sec)	LWR/P Image N°	Exp. Time (min:sec)	FES cts.s^{-1}
79 Jul 30	4085.5	5991	135:08	R 5218	120:00	100.0 ± 2.5
79 Dec 31	4238.7	7508	75:00	6499	186:00	88.0 ± 2.5
80 May 29	4388.5	9145	185:00	7884	115:00	73.5 ± 2.5
81 Jan 31	4636.0	11201	110:00	9818	42:00	77.0 ± 2.5
81 May 07	4731.5	13915	216:00	10539	180:00	79.0 ± 2.5
81 May 16	4740.5	13974	287:00	10622	160:00	81.5 ± 2.5
83 Jun 16	5502.5	20237	223:00	16177	160:00	77.9 ± 2.5
84 Feb 02	5732.8	22186	167:00	P 2731	120:00	75.7 ± 2.5
84 Feb 05	5735.8	22207	210:00	2741	112:00	79.5 ± 2.5
85 Feb 11	6107.7	25213	263:00	5348	150:00	77.2 ± 2.5
85 Feb 15	6111.7	25249	270:00	5371	140:00	77.8 ± 2.5
85 Feb 19	6115.8	25277	259:00	5394	130:00	78.9 ± 2.5
85 Feb 23	6119.7	25302	281:00	5411	130:00	76.2 ± 2.5
85 Feb 27	6123.6	25329	203:00	5430	120:00	76.2 ± 2.5
85 Jun 24	6241.4	26252	290:00	6266	134:00	77.6 ± 2.5
85 Jun 29	6246.4	26314	287:00	6300	130:00	77.1 ± 2.5
85 Jul 04	6251.4	26347	291:00	...	...	73.8 ± 3.5
86 Jan 10	6440.8	27489	180:00	...	...	88.1 ± 2.5
87 Jun 25	6972.4	31250–4	675:00[a]	...	...	82.8 ± 2.5
87 Dec 10	7140.1	32496	171.0	...	...	91.3 ± 3.5
87 Dec 14	7143.9	32520–4	600:00[b]	12278-9	198:00[c]	94.7 ± 2.5

[a]Total time: three exposures of 115 min and two exposures of 165 min.
[b]Total time: five exposures, 120 min each.
[c]Total time: two exposures of 105 and 93 min, respectively.

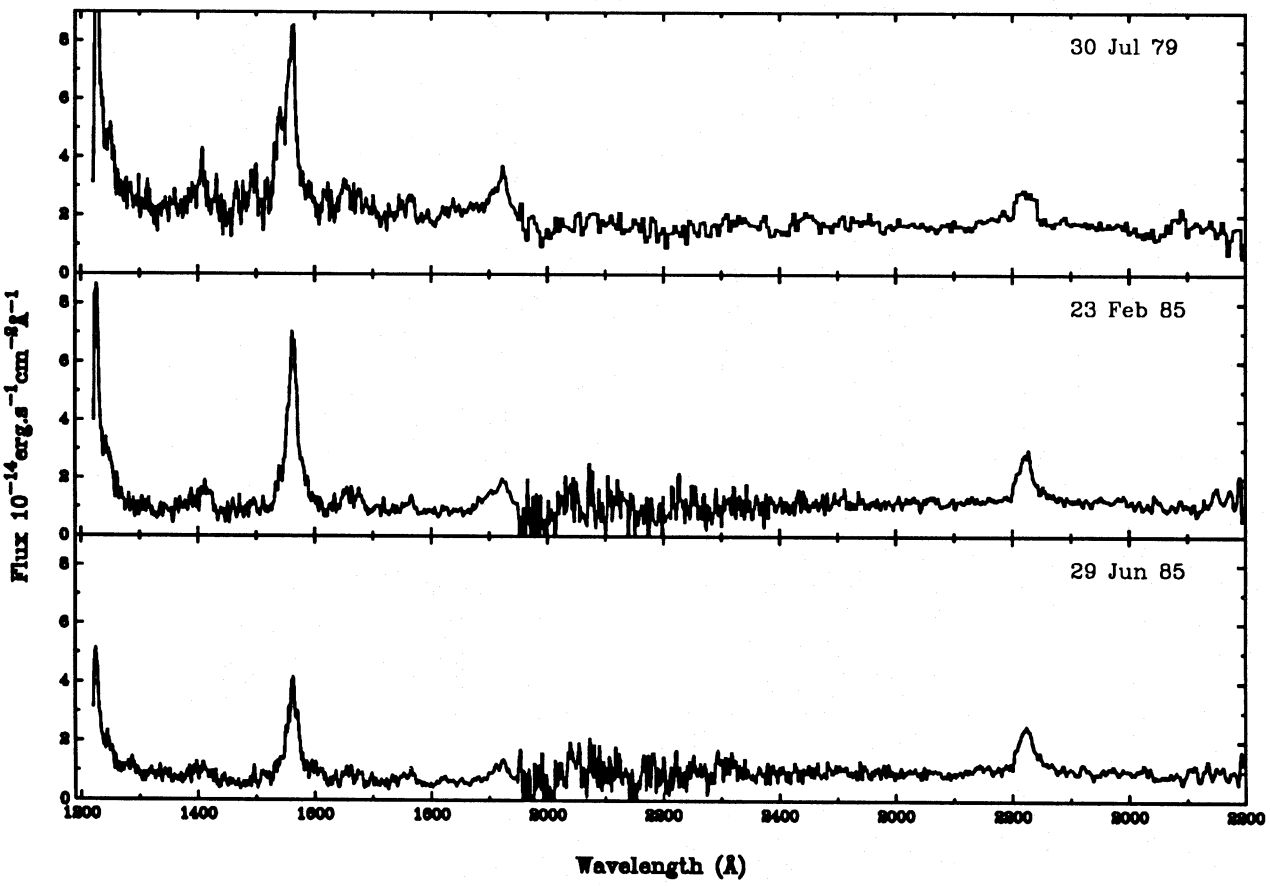

Figure 1. Three representative (high, mean and low activity states) UV spectra.

Table 7. Dereddened $[E(B-V)=0.029]$ UV continuum flux.

JD	$F_{1333\text{Å}}$ 16 Å	$F_{1447\text{Å}}$ 26 Å	$F_{1726\text{Å}}$ 24 Å	$F_{1803\text{Å}}$ 16 Å	$F_{2011\text{Å}}$ 38 Å	$F_{2227\text{Å}}$ 46 Å	$F_{2710\text{Å}}$ 30 Å	$F_{3031\text{Å}}$ 36 Å
4085.5	2.73±.13	2.54±.20	2.44±.18	2.26±.10	1.94±.33	1.87±.34	1.97±.12	1.60±.14
4238.7	1.48±.25	0.36±.35	1.11±.60	1.18±.21	1.02±.37	0.83±.43	1.10±.09	1.07±.29
4388.5	1.26±.13	1.26±.17	0.99±.18	1.12±.10	0.80±.28	1.15±.23	1.21±.11	1.25±.17
4636.0	1.13±.13	1.02±.17	1.26±.18	1.15±.10	1.35±.70	1.05±.40	1.46±.09	1.19±.15
4731.7	1.23±.13	1.46±.17	1.43±.18	1.55±.10	1.57±.25	1.43±.25	1.59±.08	1.37±.08
4740.5	1.05±.13	0.96±.17	1.11±.18	1.13±.10	0.93±.30	1.01±.23	1.29±.06	1.30±.05
5502.6	1.60±.13	1.52±.17	1.74±.18	1.65±.10	1.47±.29	1.42±.19	1.48±.06	1.29±.14
5732.9	1.57±.13	2.07±.17	1.67±.18	1.53±.10	1.14±.38	1.30±.48	1.54±.07	1.41±.06
5735.8	0.81±.13	0.92±.17	0.90±.18	1.07±.10	0.79±.41	1.60±.32	1.50±.15	1.23±.07
6107.9	1.04±.13	1.01±.17	1.21±.18	1.00±.10	0.94±.81	1.57±.52	1.54±.08	1.31±.12
6111.8	1.22±.13	0.96±.17	0.94±.18	1.05±.10	0.23±.74	1.16±.67	1.46±.08	1.30±.13
6115.9	1.57±.13	1.34±.17	1.24±.18	1.34±.10	0.85±.76	1.48±.46	1.47±.11	1.30±.13
6119.7	1.00±.13	1.01±.17	1.16±.18	1.06±.10	0.90±.62	1.43±.59	1.41±.12	1.30±.17
6123.8	0.86±.13	0.64±.17	0.68±.18	0.76±.10	0.66±.67	1.19±.48	1.17±.13	1.03±.14
6241.4	0.88±.13	0.85±.17	0.87±.18	0.91±.10	0.63±.71	1.26±.39	1.11±.07	1.02±.08
6246.5	1.12±.13	0.79±.17	0.78±.18	0.65±.10	0.63±.69	1.08±.46	1.11±.07	1.15±.16
6251.4	0.66±.13	0.64±.17	0.68±.18	0.64±.10	...	...	...	...
6440.8	2.19±.13	1.86±.17	1.85±.18	1.83±.10	...	...	...	...
6972.4	1.12±.06	1.24±.07	1.32±.09	1.32±.05	...	...	...	...
7140.1	2.73±.13	2.39±.17	2.33±.18	2.18±.10	...	...	...	...
7143.9	2.47±.06	2.54±.07	2.73±.09	2.49±.05	2.77±.66	2.14±.63	2.12±.08	1.98±.15

Fluxes in units of 10^{-14} erg s^{-1} cm^{-2} Å^{-1}.

Table 8. Dereddened $[E(B-V)=0.029]$ flux of the strong UV emission lines.

JD	Lyα λ1216 1224-1264 Å	C IV λ1550 1512-1610 Å	C III]+Si III] 1895-1945 Å	Mg II λ2800 2800-2850 Å	Fe II (UV) 2000-3000 Å
4085.5	382±14	246±11	59±6	58±9	293±70
4238.7	214±29	234±22	46±12	59±9	453±139
4388.5	232±14	184±11	47±6	50±9	252±130
4636.0	194±14	148±11	37±6	45±17	457±139
4731.7	326±14	216±11	43±6	55±9	471±70
4740.5	209±14	143±11	37±6	45±9	354±70
5502.6	244±14	177±11	23±6	53±9	363±70
5732.9	289±14	159±11	27±6	63±9	284±117
5735.8	242±14	165±11	34±6	54±9	368±70
6107.9	273±14	177±11	39±6	55±9	373±70
6111.8	230±14	191±11	48±6	59±9	375±70
6115.9	265±14	171±11	29±6	53±9	288±70
6119.7	299±14	196±11	42±6	61±9	399±70
6123.8	168±14	173±11	43±6	60±9	328±70
6241.4	166±14	119±11	30±6	53±9	324±70
6246.5	149±14	118±11	28±6	57±9	343±70
6251.4	150±14	102±11	26±6	...	...
6440.8	345±14	225[a] ±12	50±6	...	...
6972.4	332± 6	235± 5	47±3	...	...
7140.1	281±14	216±11	44±6	...	...
7143.9	376± 6	245± 5	40±3	68±9	613±70

Intensities in units of 10^{-14} erg s^{-1} cm^{-2}.
[a]Bright spot on top of the line.

1987 December 10, when only one SWP spectrum was obtained. Table 6 lists the mean count rate for each epoch. The errors represent the mean of the standard deviations at each epoch, averaged over all epochs for which more than one measurement is available. This mean error was further multiplied by $\sqrt{2}$ on 1985 July 4 and 1987 December 10. All counts recorded after 1982 were corrected for the 3 per cent per year sensitivity loss of the FES photocathode, as documented by Barylak, Wasatonic & Imhoff (1985).

2.3.2 *Broad-band imaging*

CCD observations of NGC 4593 were obtained with three broad-band filters (U, V and I) in the 1.5-m JKT telescope at the Roque de los Muchachos in La Palma. The images were taken on two consecutive nights (1988 March 9 and 10), and at least twice with each filter: one with a short exposure time to avoid problems with saturation of the nucleus and another one of longer exposure, to ensure a

good signal in the disc of the galaxy. The seeing was ~1 arcsec. The calibration procedure, except for the absolute flux part of it, was standard. Owing to the non-photometric conditions during the nights, the latter was performed using the *UBVRI* photoelectric photometry of Hamuy & Maza (1987). They report accurate measures of the NGC 4593 flux in two different apertures (17 and 24 arcsec) and at four different epochs. In order to avoid the variable nucleus, we use the flux from the annulus between 17 and 24 arcsec to calibrate our images. An independent test of the accuracy of the calibration is provided by the multi-aperture broad-band photometric observations of McAlary et al. (1983). They measured the NGC 4593 flux throughout four apertures (ranging from 7.5 to 31.8 arcsec) in the *UBVRI* bands on 1980 April 17. Following the same procedure as for the Hamuy & Maza data, we found that the calibration constants agreed to better than 0.1 mag (e.g. ≤10 per cent in fluxes).

2.3.3 *Long-slit spectroscopy: the off-nuclear spectrum*

To account for the stellar SED, long-slit optical spectra of the Hβ λ4861 region were obtained with the 2.5-m Isaac Newton Telescope (INT) at the Observatorio del Roque de los Muchachos on the island of La Palma (Spain), on 1988 March 9. The detector used was the IPCS, with the Intermediate Dispersion Spectrograph on the Cassegrain focus. The slit width was ~1.0 arcsec, while the spatial resolution along the slit was 1.512 arcsec per pixel and the spectral resolution ~1 Å. It was placed at two different position angles (e.g. 0° and 308°), in order to investigate the existence of any spatial structure in the nuclear regions of NGC 4593. Long exposures (e.g. 3000 s) were aimed at obtaining sufficient signal in the off-nuclear region. The calibration was performed using standard routines of the FIGARO Starlink package. The effects of differential atmospheric refraction plus the IPCS S-distortion were carefully corrected for. The final wavelength calibration is accurate to 0.1 Å. The flux calibration was performed using standard stars. As none of the nights was of photometric quality, calibration curves obtained with two different standards agree to within ≤10 per cent in the central part of the spectrum, but only to within 20–25 per cent in the blue (3400–3900 Å).

The two long exposure time-frames have strong signal ($\geq 3\sigma$) outside the nucleus (at least in the 11 central scans) and, in both, narrow- and broad-line emission is confined to the three central scans. Moreover, the narrow-to-broad-line intensity ratio is independent of the distance to the nucleus in these three scans. Given the slit width (~1 arcsec) – similar to the diameter of the seeing disc – we are therefore quite confident that this signal is mostly nuclear light scattered by the slit, the atmosphere and the instruments. The remaining scans show typical late-type stellar population spectra and no extended narrow-line emission. We have extracted two spectra, centred at 5.29 arsec above and below the nucleus, and averaged them. This is the off-nuclear NGC 4593 spectrum that will be used in Section 3 to compare with that of the bulge in a normal spiral.

2.3.4 *Nuclear spectroscopic observations*

Details of the optical spectroscopic observations are summarized in Table 9. Optical spectra were obtained in 1984 January and 1985 February at ESO, Chile, with the Boller & Chivens spectrograph, together with the Image Dissector Scanner (IDS). The IDS has two 4×4 arcsec^2 apertures, which allow simultaneous recording of the sky and object spectrum. The apertures were swapped every 5 min to ensure an accurate background subtraction. The reduction was conventional and the flux was calibrated against Oke's standard stars observed during the same night. An additional spectrum was obtained on 1988 March 14, with the Ohio State University Image Dissector Scanner (Byard et al. 1981) on the 1.8-m Perkins reflector of the Ohio State and the Ohio Wesleyan Universities at the Lowell Observatory. Simultaneous spectra of NGC 4593 and the sky background were obtained through circular apertures of projected diameter 7 arcsec. Data acquisition and reduction procedures are described in Peterson (1987).

While the use of large spectrograph entrance apertures ensures that the flux from the entire narrow-line region enters the spectrograph, an undesirable side effect is that a significant amount of starlight contaminates the spectrum of the AGN. This problem is particularly troublesome in the case of a relatively faint Seyfert nucleus such as that of NGC 4593. It is possible, however, to account for the stellar contribution by subtracting a suitably scaled spectrum of the central regions of a non-active galaxy (e.g. Koski & Osterbrock 1976; Antonucci & Cohen 1983; Crenshaw & Peterson 1985; Wamsteker et al. 1990). In this case, the spectrum of the early spiral M31 is a good match to the NGC 4593 off-nuclear spectrum (Section 3) and, hence, it has been used to model the stellar contribution. The procedure followed to estimate and remove the stellar flux from the optical spectra is described in the next section.

Table 9. Log of optical spectroscopic observations.

Date (U.T.)	JD-2,440,000	Time (U.T.)	Exp. (min:sec)	Tel.	Range (Å)	Resol. (Å)	Seeing (″)	Notes
31 Jan 84	5730.80	07:15	21:00	3.60m	3640–5990	7	2.0	Photometric
15 Feb 85	6111.97	11:17	30:00	1.52m	4150–7665	10	1.5	Photometric
16 Feb 85	6112.97	11:09	60:00	1.52m	4550–5750	3	1.5	Photometric
23 Feb 85	6119.98	11:24	40:00	1.52m	4150–7665	10	3.0	Not Photom.
24 Feb 85	6120.97	11:09	60:00	1.52m	4550–5750	3	1.5	Photometric
25 Feb 85	6121.97	11:21	60:00	1.52m	6210–7450	3	2.0	Nearly Phot.
14 Mar 88	7234.89	09:20	60:00	1.8m	4000–6000	10		

Prior to measuring the flux of the optical lines, we also removed the underlying power-law continuum, as well as the strong Fe II line spectrum, by modelling its emission over the entire ultraviolet–optical range, as explained in Section 4. Deblending techniques were then used to measure the flux of the Balmer lines (Appendix A). The measured optical line intensities are listed in Table 10. The uncertainties quoted result from the propagation of the errors of the Gaussian parameters in the fit. They do not take into account the error due to the uncertainty in the flux calibration or the errors introduced by the subtraction of the power-law and Fe II line spectra. The intensity of Fe II multiplet 42 (4800–5450 Å) is also listed separately, to illustrate the strength of individual iron features.

Since the narrow-line region is too extended to vary over time-scales of a few years, one can use the [O III] line to check the calibration. The mean (dereddened) [O III] λ5007 flux is 12.2×10^{-14} erg s^{-1} cm^{-2}, with an rms dispersion of 1.3×10^{-14}, showing that our flux calibration is, on average, accurate to about 10 per cent. We have compared our line fluxes with others reported in the literature. McAlpine et al. (1979) quoted 17×10^{-14} erg s^{-1}cm^{-2} for the [O III] λ5007 flux, uncorrected for reddening. Morris & Ward (1988) obtained the same value with an error of $\leq$30 per cent. Correction for reddening raises these values by 10 per cent to 18.6×10^{-14} erg s^{-1} cm^{-2}. Dahari & De Robertis's (1988) dereddened flux is 12.1×10^{-14} erg s^{-1}cm^{-2}, whilst that of Kollatschny & Fricke (1985) is 27.2×10^{-14} erg s^{-1}cm^{-2}. The latter authors quoted a flux for the [S II] $\lambda\lambda$6717, 6731 line which is also larger than ours by a factor of 1.6. If we leave aside the result of Kollatschny & Fricke, our [O III] $\lambda\lambda$4959, 5007 flux agrees reasonably well with those in the literature. The larger value obtained by McAlpine et al. and Morris & Ward can be entirely accounted for by the fact that these authors included the board Fe II base underneath the [O III] line in their measurement.

2.5 IR photometry

Near-IR, *J*, *H*, *K*, and *L* photometry was carried out at SAAO (Sutherland) at 22 different epochs, from 1982 April to 1987 July. The 1.9-m telescope was used with either the MkII or MkIII photometer. The aperture diameter was 12 arcsec. Additional larger-aperture data were also recorded at some epochs using the MkII photometer on the 0.75-m telescope, in order to estimate the contribution of the underlying galaxy as a function of wavelength and aperture size. All the data have been reduced to the revised SAAO standard system (Carter 1990). The properties of the photometers and the photometric systems are discussed in Glass (1984). The statistical error in the *JHK* bands for an individual measurement is $\leq$0.01–0.02 mag. To account for possible systematic errors, we adopt a formal uncertainty of $\pm$0.03 mag at *JHK* and $\pm$0.05 at *L*, except where the statistical errors are larger. Table 11 lists the observing dates and the fluxes measured through a 12-arcsec aperture.

3 THE CONTRIBUTION OF THE UNDERLYING GALAXY

3.1 Estimation of the flux from stars and dust in the galaxy

In order to analyse the stellar light contaminating the nuclear spectra of NGC 4593, we have analysed the surface brightness distribution in the galaxy underlying the active nucleus. The broad-band images described in Section 2.3.2 have been used. The position of the nucleus in each frame is determined by fitting a two-dimensional Gaussian to the central pixels. Radial profiles are measured by adding the flux in circular rings centred on the nucleus. Circular profiles are used instead of elliptically averaged ones because the eccentricity of the outer isophotes of NGC 4593 is close to 1 ($b/a\approx0.7$, as found by us and previously by Grosbøl 1985). As

Table 10. Dereddened [$E(B-V)=0.029$] optical line fluxes.

Line	Civil Date					
	30 Jan 84	15 Feb 85	16 Feb 85	24 Feb 85	25 Feb 85	14 Mar 88
Hγ	11.34±0.71	14.09±0.69	···	···	···	16.08±0.59
[*OIII*]λ4361	1.39±0.18	1.49±0.21	···	···	···	2.41±0.27
HeIIλ4686	11.0±1.7	10.2±1.4	10.7±1.2	16.1±2.6	···	8.91±0.98
HβNarr	0.94±0.21	0.68±0.23	1.08±0.21	0.99±0.25	···	···
HβBroad	35.5±1.4	36.1±1.2	40.4±1.6	35.7±2.1	···	42.8±0.9
[*OIII*]λ4959	4.43±0.23	4.08±0.24	4.39±0.24	3.43±0.29	···	3.84±0.26
[*OIII*]λ5007	13.04±0.40	12.33±0.42	13.74±0.42	10.27±0.50	···	11.68±0.45
FeII m42	66±12	69±11	67±18	53±24	···	55±19
HeIλ5875 B	9.14±0.88	15.5±1.4	···	···	···	28.3±3.0
[*NII*]λ6548	···	4.11±0.33	···	···	1.11±0.42	···
Hα N	···	9.29±0.49	···	···	7.02±0.70	···
Hα B	···	122.4±2.6	···	···	136.8±4.0	···
Hα R	···	9.23±2.2	···	···	5.5 ±3.4	···
[*NII*]λ6584	···	8.11±0.92	···	···	4.0 ±1.5	···
[*SII*]λ6717	···	1.90±0.18	···	···	1.86±0.47	···
[*SII*]λ6731	···	1.69±0.17	···	···	1.72±0.45	···

Intensities in units of 10^{-14} erg s^{-1} cm^{-2}.

discussed by MacKenty (1990), the correction for the use of circularly averaged profiles in the central surface brightness of the disc is found empirically to be less than 0.2 mag in R for $0.6 < b/a < 0.8$. Moreover, Boroson (1981) pointed out that the elliptically averaged profile is slightly incorrect near the centre, as a result of the smaller eccentricity of the bulge (i.e. more spherical than the disc) which dominates in the central regions. The amplitude of this effect is similar to the previous one: ≤ 0.2 mag, but with the opposite sign, and therefore there is no need to use elliptically averaged profiles for NGC 4593.

The spatial distribution of the luminosity in normal spiral galaxies has been studied previously by several authors (see e.g. Boroson 1981 and references therein). It is generally assumed that it can be explained in terms of two contributions: one for the disc and another one for the bulge, the latter being dominant in the central ≈ 1 kpc and the former being dominant in the outer regions. The bulge is usually well fitted by a de Vaucouleurs law of the form $\mu = \mu_e + 8.325\,[(r/r_e)^{1/4} - 1]$, in mag arcsec^{-2}, where r_e is the effective radius inside which half of the light is contained, and μ_e is the surface magnitude at this radius. For the disc, an exponential law, $\mu = \mu_0 + 1.0857 r/r_0$, is used. The parameter r_0 is the scalelength of the exponential and μ_0 is the central surface brightness. We have fitted both components using the iterative method described by Boroson, i.e. fitting each component (bulge or disc) in the regions where it dominates the galaxy luminosity distribution. The bulge is fitted from 4 to 14.5 arcsec. For the disc, we find that the inner radius of the region in which the mean intensity can be approximated by an exponential is $r \geq 26$ arcsec, in agreement with Grosbøl (1985). The outermost radius is determined by the signal-to-noise ratio in the frame: ≈ 50 arcsec (3σ limit) in the V and I bands, and ≈ 34 arcsec in U. Given the large uncertainties in the U disc profile, its scalelength is fixed to the mean V and I ones. The best-fitting parameters are shown in Table 12, together with the disc surface brightnesses corrected by reddening in the line of sight [$E(B-V) = 0.029$] and by disc inclination ($i = 47°$; Grosbøl 1985).

Table 11. Near-IR dereddened [$E(B-V) = 0.029$] fluxes.

JD	J	H	K	L
-2,440,000		mJy		
5081	58.2± 1.6	77.8± 2.1	76.0± 2.1	···
5343	56.6± 1.5	76.4± 2.1	81.1± 2.2	···
5419	55.1± 1.5	75.7± 2.0	73.2± 2.0	77.8± 4.9
6111	58.7± 1.6	84.6± 2.3	90.5± 2.4	92.7± 6.0
6112	58.7± 1.6	83.8± 2.3	87.3± 2.4	101.7± 4.1
6114	57.1± 1.5	80.8± 2.2	84.1± 2.3	86.9± 4.8
6116	57.1± 1.5	83.0± 2.2	85.7± 2.3	94.4± 7.4
6117	56.6± 1.5	80.8± 2.2	84.1± 2.3	79.3± 4.8
6120	58.2± 1.6	82.3± 2.2	81.1± 2.2	89.4± 3.8
6122	56.6± 1.5	80.0± 2.2	80.3± 2.2	84.6± 6.9
6194	53.1± 1.4	70.3± 1.9	70.0± 1.9	71.6± 3.3
6195	54.6± 1.5	77.1± 2.1	71.9± 1.9	77.8± 3.4
6199	53.1± 1.4	74.3± 2.0	71.9± 1.9	67.2± 3.4
6477	58.7± 1.6	81.5± 2.2	82.6± 2.2	79.3± 5.5
6478	59.3± 1.6	83.8± 2.3	83.3± 2.2	82.3± 5.5
6479	58.2± 1.6	82.3± 2.2	81.8± 2.2	79.3± 5.4
6582	59.8± 1.6	92.7± 2.5	97.5± 2.6	108.4± 5.5
6609	61.5± 1.7	89.4± 2.4	95.7± 2.6	91.0± 6.4
6845	60.4± 1.6	87.7± 2.4	93.9± 2.5	111.5± 4.4
6923	58.7± 1.6	83.0± 2.2	86.5± 2.3	101.7± 4.1
6985	60.9± 1.6	86.1± 2.3	87.3± 2.4	102.6± 4.1
6988	60.4± 1.6	83.0± 2.2	85.7± 2.3	92.7± 4.0

The stellar fluxes at J, H, K, L are 45, 60, 46 and 26 mJy, respectively, and are *not* subtracted.

Table 13 lists the obtained (bulge + disc) V fluxes as a function of the aperture radius, as well as those in the plane of the galaxy. The values of the galactic fluxes within $r = 2.26$ arcsec (and corrected by disc inclination and interstellar reddening) are listed in the last column of Table 12. They account for the flux through a square 4×4 arcsec^2 aperture.

In order to extend the wavelength range, the NGC 4593 off-nuclear spectrum (Section 2.3.3) is compared with that of the bulge in M31 (an early spiral of the same morphological type as NGC 4593, Sb). The M31 template is scaled to the NGC 4593 stellar emission through a rectangular slit having the size and centred at the position of the averaged scans, as measured in the V image described above. The result is shown in Fig. 2. The off-nuclear stellar spectrum in NGC 4593 matches quite well the M31 template, both in shape and intensity. Incidentally, this confirms the consistency of the V-band image and long-slit CCD spectra absolute calibrations. This procedure shows that, depending on the level of activity, between 70 and 85 per cent of the total flux at 5640 Å in the ESO spectra is due to the composite stellar population in the bulge of NGC 4593.

To estimate the galaxy contribution within 12 arcsec in the IR, we follow the Glass (1992) procedure for NGC 3783. The 12-arcsec *JHKL* fluxes are all linearly correlated against each other (Paper 2 and Fig. 3). As discussed by Glass, the H versus K is the most reliable relationship. It has been fitted by a straight line with the method recommended by Isobe et al. (1990). The extrapolation of the best-fitting line to a line representing the underlying galaxy $H-K$ colour gives the H and K fluxes of the galaxy within this aperture (Fig. 3). To

Table 12. Galaxy parameters.

Band	Bulge			Disk		B+D
	r_e	μ_e	r_0	μ_0	μ_{0c}	r=2″.26
	″	mag/⊔	″	mag/⊔	mag/⊓	mJy
U	10.7±3.4	22.2±0.3	47.2±8.	24.0±0.2	24.3±0.2	.750
V	18.8±2.0	21.7±0.1	47.2±8.	21.9±0.3	22.3±0.3	4.85
I	20.8±4.8	20.1±0.3	47.2±8.	21.8±0.3	22.2±0.3	9.94
	Kpc	μ_{ec}	Kpc			
B	2.7±0.6	22.7 ±0.1	7.5±1.4	22.3 ±0.3	22.7±0.3	

Table 13. Stellar (dereddened) fluxes in the V band.

Radius	$Flux_{obs}$	$Flux^{a}_{corr}$
"	mJy	
0.5	0.1 ± 0.7	0.1 ± 0.7
1.0	1.4 ± 0.7	1.4 ± 0.7
1.5	2.8 ± 0.4	2.8 ± 0.4
2.0	4.1 ± 0.4	4.1 ± 0.4
2.5	5.5 ± 0.5	5.5 ± 0.5
3.0	6.9 ± 0.8	6.8 ± 0.8
3.5	8.2 ± 1.1	8.1 ± 1.1
4.0	9.5 ± 1.3	9.4 ± 1.3
4.5	10.7 ± 1.3	10.6 ± 1.3
5.0	11.9 ± 1.4	11.8 ± 1.4
5.5	13.1 ± 1.4	12.9 ± 1.4
6.0	14.2 ± 1.4	14.0 ± 1.4
6.5	15.3 ± 1.4	15.1 ± 1.4
7.0	16.4 ± 1.5	16.1 ± 1.5
7.5	17.5 ± 1.5	17.1 ± 1.5
8.0	18.5 ± 1.6	18.1 ± 1.6
8.5	19.5 ± 1.7	19.1 ± 1.7
9.0	20.5 ± 1.7	20.0 ± 1.7
9.5	21.5 ± 1.8	20.9 ± 1.8
10.0	22.4 ± 1.8	21.8 ± 1.8
10.5	23.3 ± 1.9	22.7 ± 1.9
11.0	24.2 ± 1.9	23.6 ± 1.9
11.5	25.1 ± 1.9	24.4 ± 1.9
12.0	26.0 ± 2.0	25.2 ± 2.0
12.5	26.9 ± 2.0	26.0 ± 2.0
13.0	27.8 ± 2.0	26.8 ± 2.0
13.5	28.6 ± 2.1	27.6 ± 2.1
14.0	29.4 ± 2.1	28.4 ± 2.1
14.5	30.2 ± 2.1	29.1 ± 2.1
15.0	31.0 ± 2.2	29.8 ± 2.2

[a]Corrected for disc inclination.

extrapolate to the J and L bands, we use the NGC 4593 non-nuclear $J-H$ colour (Table 14) and $K-L=0.22\pm0.02$ (Glass 1984). One finds $F_J=45\pm10$ mJy, $F_H=60\pm12$ mJy, $F_K=46\pm9$ mJy and $F_L=26\pm6$ mJy (where the errors come from the propagation of the uncertainties in the IR colours plus those on the slope and independent term of the F_H versus F_K regression line). This translates into average relative stellar contributions of 80, 73, 55 and 40 per cent at J, H, K and L, respectively.

To check the consistency of the two methods (i.e. luminosity profile fitting and colour–colour diagrams), we extrapolate the V fluxes through a 12-arcsec diameter aperture to the IR and verify that they agree with the above results. Previously, we measured the $V-K$ colour of the galaxy in NGC 4593 using our V CCD frame and the multi-aperture K data (Table 14). We found $V-K=3.35\pm0.12$ (rms), which is not significantly different from the standard $V-K=3.22\pm0.10$ (Glass 1984). The near-IR galactic flux through any other aperture can be estimated by extrapolating the V flux to the K band and using $V-K=3.22$.

To infer a lower limit to the galaxy contribution to the *IRAS* measurements at 12 and 25 μm, we use ground-based, smaller-aperture (e.g. 5 arcsec) observations of Ward et al. (1987) at 10 and 20 μm, following the Edelson & Malkan (1986) procedure. They assume that all the flux within the smaller aperture is non-stellar in nature and then extrapolate it from 20 to 25 μm, assuming a power-law spectral shape of this component with an index $\alpha=-1$. The extranuclear flux at 25 μm is extrapolated to 100 μm, assuming the far-IR spectral shape found by de Jong et al. (1984) for a sample of non-active galaxies ($\alpha_{FRI}=-1.5$). At least 50 per cent of the *IRAS* 100-μm flux is found to come from the stars in the galaxy. The lower limit to the stellar flux contribution is estimated to be 63 per cent at 20 μm by Ward et al. (1987), after interpolating the 10- and 25-μm *IRAS* fluxes to 20 μm and comparing with their ground-based 5-arcsec 20-μm

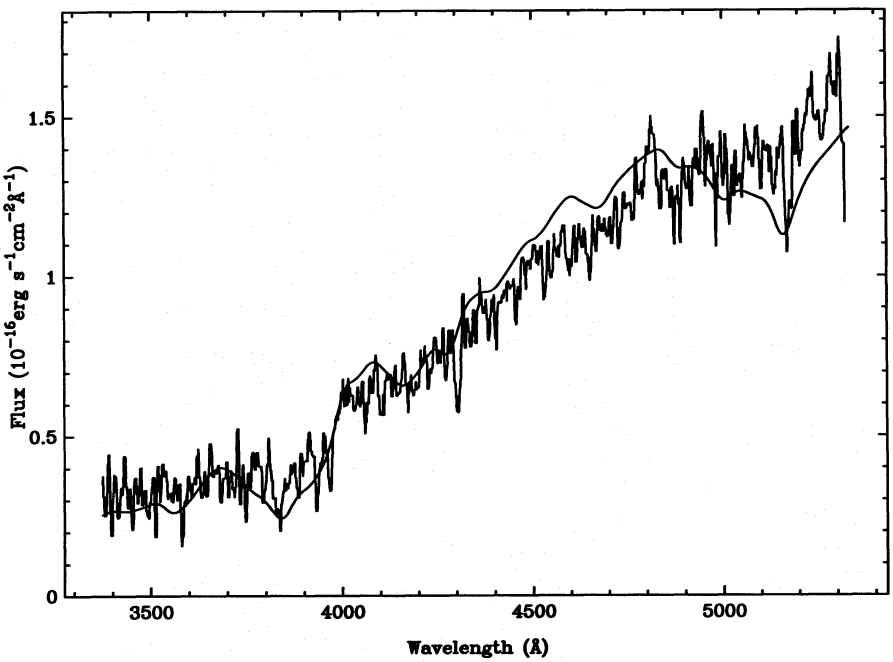

Figure 2. The NGC 4593 off-nuclear optical spectrum and, superimposed, the M31 template scaled to the NGC 4593 luminosity through the slit as measured in the V image (see text for more details).

measurement. The uncertainties of these estimates are large, as reflected by the fact that Devereux (1987) finds a much lower proportion of extended flux relative to central flux (i.e. 27 per cent) using the NGC 4593 10-μm flux through a similar aperture (5.5 arcsec).

3.2 Comparison with other works

To check the validity of our results, we compare them with those reported in the literature either for NGC 4593 or for other spirals. The results of the comparison are summarized in Table 15. All the measurements have been corrected to $H_0 = 75$ km s^{-1} Mpc^{-1}. The luminosity profile parameters have been corrected for disc inclination and interstellar reddening.

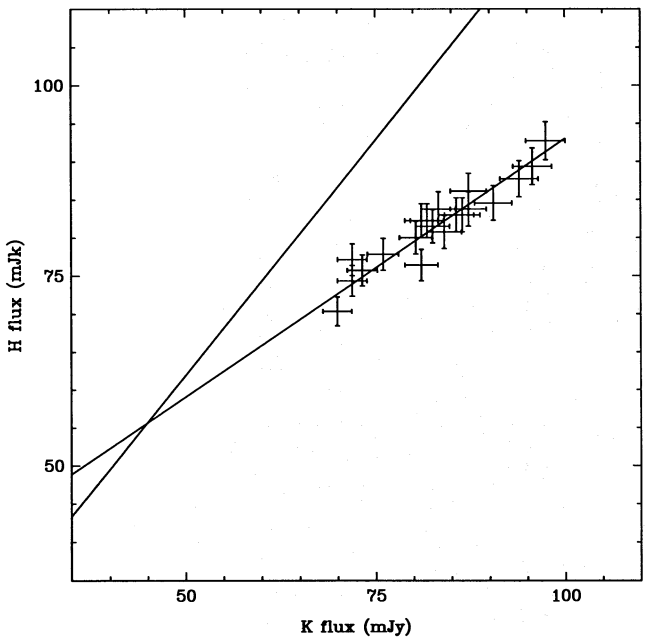

Figure 3. The dereddened infrared H flux plotted against the K flux and the straight line fitted to these points. The second line represents the underlying galaxy $H-K$ colour in NGC 4593 (i.e. $H-K=0.27$). The intersection of both lines yields its non-nuclear flux for a 12 arcsec aperture.

The work of Grosbøl (1985) is a morphological analysis of the discs of some spirals, including NGC 4593; only the result for this galaxy is shown in Table 15. Freeman (1970) studied a sample of 36 normal spirals, Boroson (1981) studied 24 normal spirals, Yee (1983) studied 20 Markarian Seyferts, Kent (1985) studied 105 intrinsically luminous galaxies (among which he has fitted the profiles of 53 spirals) and MacKenty (1990) studied 51 Seyferts. To estimate the B magnitudes in NGC 4593, we use V magnitudes and $B-V=0.72$ for the disc (an average of Yee's mean value of $B-V=0.70\pm0.14$ in a ring just outside the nucleus – from 7 to 15 arcsec – and MacKenty's 0.75 ± 0.17 for an annulus between 5 and 10 kpc) and $B-V=0.9$ for the bulge (Boroson 1981). Inspection of Table 15 shows that the scalelengths for both the disc and the bulge in NGC 4593 are comparable to those of other galaxies.

We also compare our estimates of the stellar flux in NGC 4593 with those from other works. Our results are fully compatible with those of Ward et al. (1987), but are smaller than those of McAlary & Rieke (1988). The latter authors already pointed out that their method tends to overestimate slightly the stellar flux. Kotilainen et al. (1992) and Kotilainen, Ward & Williger (1993) have performed decomposition of the IR and optical luminosity profiles of NGC 4593, based on broad-band images. Using their parameters, we compute the *JHK* galaxy fluxes through an $r=6$ arcsec aperture and list them in Table 15. Within the admittedly large uncertainties, their results agree well with ours. The Kotilainen et al. (1992, 1993) uncertainty is manifested in the large dispersion for the values of their best-fitting parameters for the bulge and the disc in a particular broad band, and in the differences between their IR and optical results.

4 Fe II LINE AND BALMER CONTINUUM EMISSION

The procedure for measuring the Balmer continuum plus Fe II contribution in the 2000–5000 Å range is similar to that

Table 14. IR multi-aperture photometry and colours.

J.D. -2440000	R_{out} "	R_{in}	K mag.	V	H-K	J-H
5343	4.5	3	11.42±0.13	14.80	0.23±0.16	0.82±0.13
5081	6	4.5	11.42±0.16	15.03	0.31±0.21	0.79±0.19
5343	6	4.5	11.50±0.18		0.45±0.24	0.67±0.22
5419	6	4.5	11.57±0.17		0.22±0.22	0.88±0.20
6120	6	4.5	11.64±0.21		0.16±0.26	0.92±0.22
5081	9	6	11.10±0.15	14.32	0.12±0.19	0.79±0.17
6111	9	6	11.00±0.16		0.24±0.21	0.76±0.17
6116	9	6	10.97±0.15		0.26±0.20	0.81±0.17
6477	9	6	11.01±0.15		0.47±0.21	0.63±0.20
5379	25.5	17	10.44±0.16	13.66	0.22±0.21	0.84±0.21
			Mean value		0.27±0.04	0.79±0.03
			Glass 1984		0.22±0.02	0.78±0.02

Magnitudes and colours corrected for reddening [$E(B-V)=0.029$].

Table 15. Comparison with other works.

Reference	Luminosity profile parameters				
	Disk		Bulge		B/D_c
	r_0 kpc	B_0 [a] mag/□	r_e kpc	B_e mag/□	
This work	7.5±1.4	22.7±0.3	2.7±0.6	22.7±0.1	0.83
Grosbøl 1985	6.4±0.2	...	...	...	...
Freeman 1970	1–5	21.65±0.30	...	...	...
Boroson 1981	1–10	21.79±0.78	0.05–3.2	21.2[b]	0.06–1.24
Yee 1983	2–8	21.3±0.5	...	...	...
Kent 1985	1.2–13	21.7±0.9	0.–5.5	22.8[b],[c]	0.01–2.34[c]
MacKenty 1990	1.5–8	21.9±1.0	...	...	...

	NGC 4593 stellar fluxes				
	V	J	H	K	L
			mJy		
This work (r=3″.75)	8.2±1.2	25±3	33±4	27±3	15±2
Ward et al. "	7.3	23	30	23	14
This work (r=54″)	12±1	35±4	48±6	39±4	22±3
MacAlary & Rieke "	16	52	69	54	35
This work (r=6″)	14±1	45±10	60±12	46±9	...
Kotilainen et al. " 1992	...	52±6	67±14	55±20	...
This work (r=3″)	2.8±0.4	...	...	...	...
Kotilainen et al. " 1993	2.84	...	...	...	...

[a] Mean values and rms deviations.
[b] Median value.
[c] Including Sb galaxies (the NGC 4593 morphological type) only.

followed by Wamsteker et al. (1990), in their decomposition of the NGC 5548 energy distribution. Using simultaneous UV and optical spectra, a power-law spectrum is fitted to the entire 1200–6500 Å range, in selected wavelength intervals that are free from emission lines. For those epochs when no simultaneous data are available, we make the assumption that the power law retains a constant spectral shape and normalize it to the value of F_{1447} measured on that date. This assumption is justified in Paper 2. After subtraction of the power law, the residual energy distribution is fairly steep, the F_λ flux rising sharply from 1600 to 3100 Å. This forces us to select those Balmer continuum models from the grid of Wills et al. (1985) whose electron temperature is 10^4 K and whose optical depth at the edge is 2.0. All other models yield a 1700–3100 Å flux ratio, which is too large compared to the observational value. The Balmer continuum intensity at each epoch is determined by scaling the model to match the observed flux density above the power law in the range 3000–3100 Å, where Fe II emission is negligible. We then fit synthetic Fe II spectra from the grid of models described in Wills et al. (1985). This is done following an iterative procedure. The synthetic Fe II spectra are convolved with a Gaussian profile whose FWHM, 4400 km s^{-1}, is that of the broad component of Hβ λ4861. The error of the total iron line + Balmer continuum flux is determined from the sum of the fit residuals added quadratically to the error on the power-law flux. The latter turns out to be the most important source of uncertainty. The resulting relative error is of the order of 15–20 per cent.

A similar iterative procedure is used to determine the strength of the optical Fe II multiples. The power law is determined either from a fit to the optical–UV SED, or – when there are no simultaneous UV data available – by scaling its intensity to the flux in the 5580–5690 Å line-free range, assuming that it retains a constant spectral shape. Fig. 4 displays the observed spectrum after removal of the stellar light and power-law continuum, together with the best-fitting synthetic Fe II spectra at each epoch. The overall procedure for decomposing the dereddened UV–optical spectrum of 1985 February 15 into its several components is illustrated in Fig. 5. The relative uncertainty on the Fe II optical line flux varies between ≈40 per cent on 1985 February 24, when the signal-to-noise ratio is the lowest, and ≈10 per cent on February 15. The validity of our decomposition is illustrated by the fact that the ([O III] λ5007/[O III] λ4959) ratio at each epoch is always close to its theoretical value of 3, the largest deviations being 3.13 and 2.98. Incidentally, it is worth noting that the broad base underneath the [O III] λ5007 line can be accounted for by Fe II multiplets, as illustrated in Fig. 4.

Inspection of Fig. 5 shows that an important fraction of the near-UV flux in NGC 4593 is due to Fe II and Balmer emission. On average, we find that as much as 64 per cent of the total 2710-Å flux is due to the sum of the two components. Indeed, the iron lines turn out to be the most

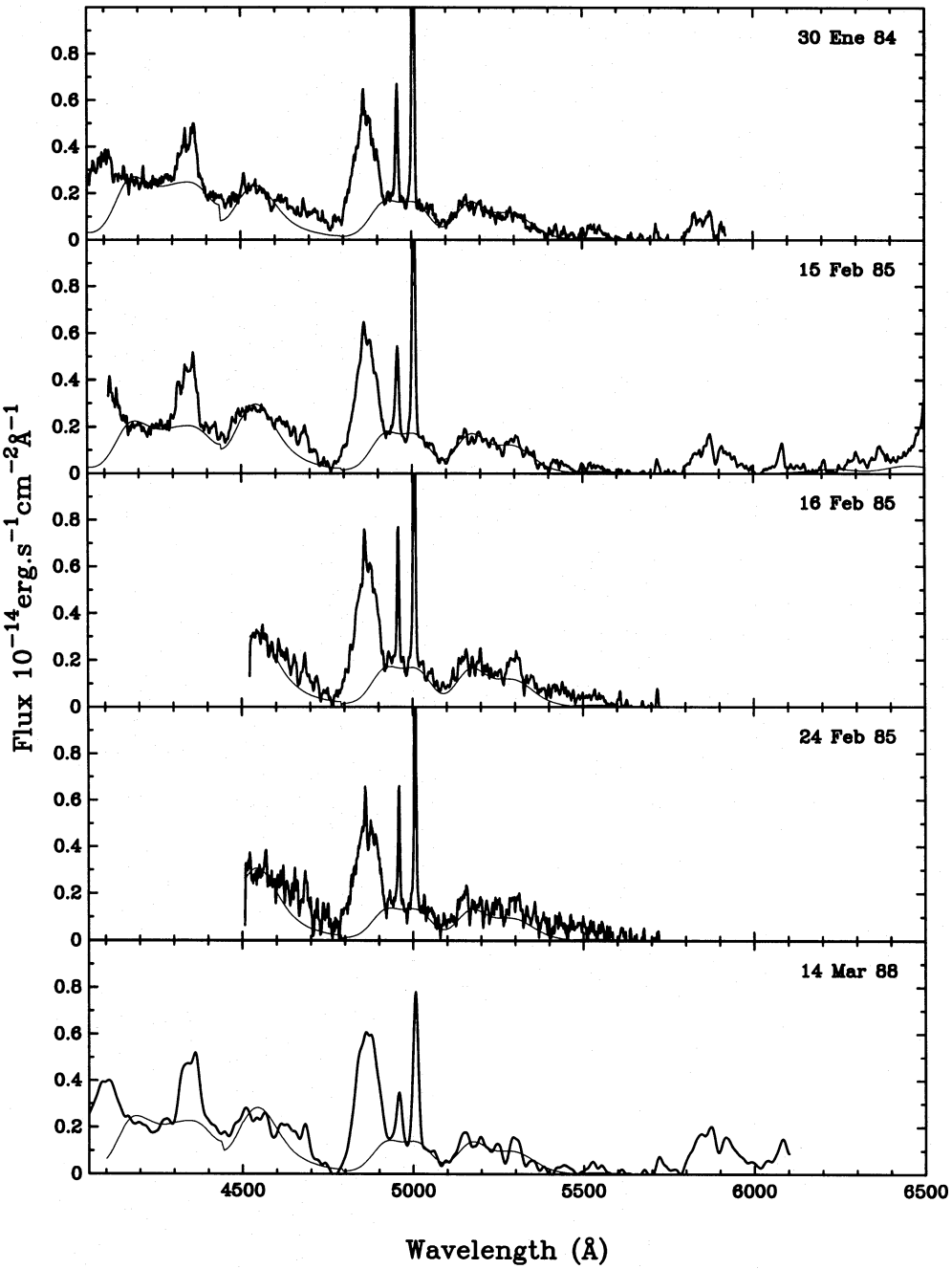

Figure 4. Dereddened optical spectra after subtraction of the underlying galaxy and power law. The Fe II emission model is plotted (thin line) together with the data.

efficient BLR cooler, their flux contributing to ~40 per cent of the total broad-line emission on 1985 February 15.

5 SUMMARY

We have presented a data set which is the result of a multi-wavelength monitoring campaign on the Seyfert 1 galaxy NGC 4593. The continuous emission has been measured from the X-rays to the IR in selected wavelength windows which are free from emission lines. The strongest UV and optical emission lines have been measured as well.

The observed continuum has been separated into different components. The 'parasitic' contributions that contaminate the pure AGN continuous emission have been modelled and their fluxes measured. It is found that dust and stars from the bulge and disc of the galaxy contribute between 70 and 85 per cent to the total light at 5640 Å. The stellar SED of NGC 4593 is similar to that of the bulge of a normal spiral galaxy of the same morphological type. Its surface brightness profile can be reproduced with a two-component model that accounts for the bulge and the disc of normal spirals. Fe II line emission represents 40 per cent of the total BLR flux in

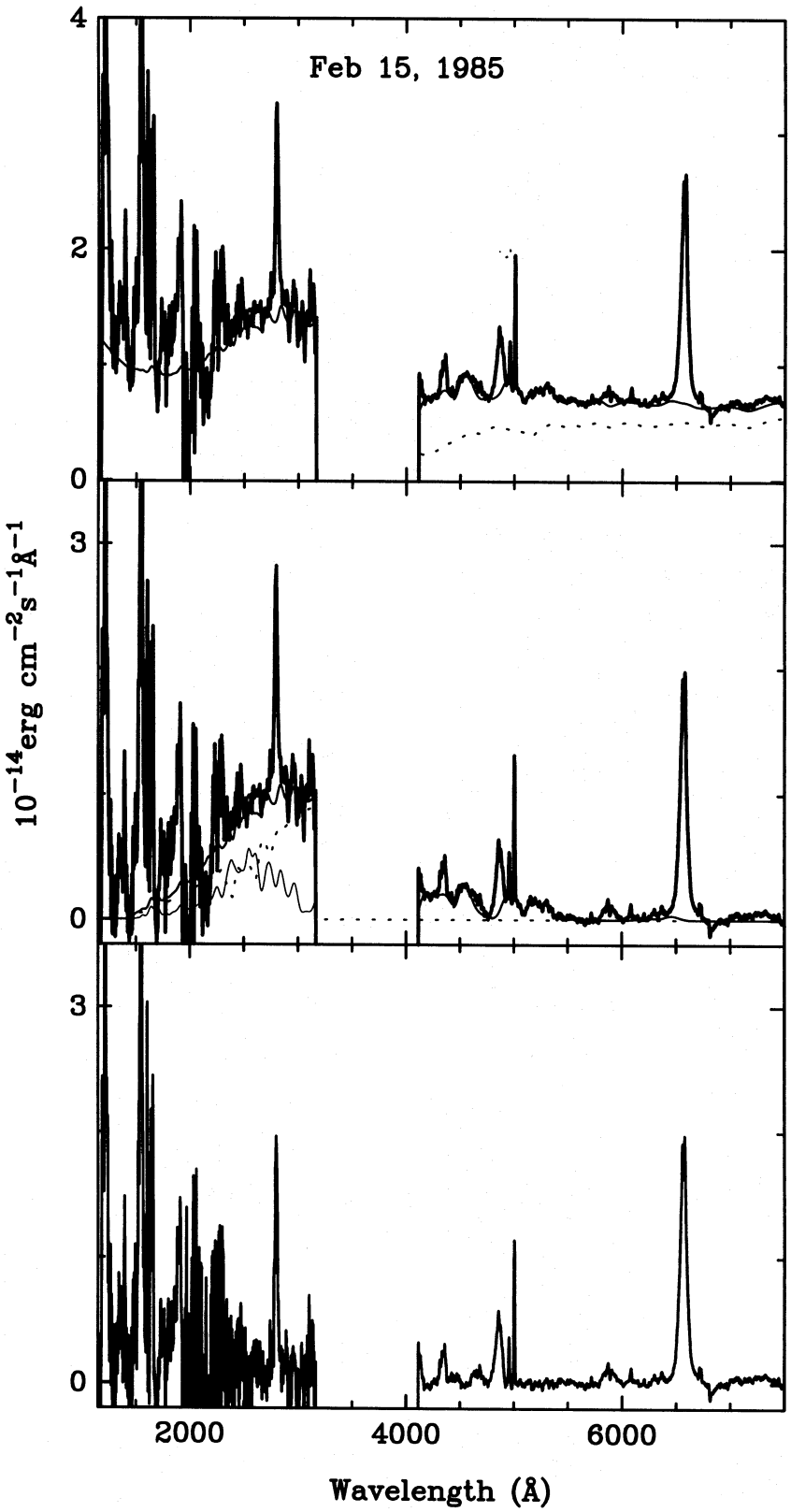

Figure 5. Decomposition of the simultaneous optical–UV spectrum of 1985 February 15. The upper panel shows the dereddened spectrum together with the total model (underlying galaxy + power law + Fe II emission + Balmer continuum; thin line), as well as the stellar component (dotted line). The middle panel shows the spectrum after subtraction of the stellar and power-law contributions, together with the model for the Fe II emission (thin line), for the Balmer continuum (dotted line) and the sum of the two (intermediate thickness line). The lower panel displays the pure emission lines that are left after subtraction of the model.

1985 February. The 2000–4000 Å 'small bump' is well accounted for by Fe II lines and Balmer continuum emission, which contributes ~64 per cent on average to the flux at 2700 Å.

ACKNOWLEDGMENTS

We thank Dr P. A. Whitelock for making some of the infrared measurements and Prof. P. O. Lindblad and Dr S. Jörsäter for their collaboration in the optical observations at La Palma.

This paper is based on observations made with the *IUE* satellite at the ESA *IUE* Observatory in Vilspa, Spain, and at the NASA Goddard Space Flight Center, observations made with the *EXOSAT* satellite, and on data collected at the European Southern Observatory, La Silla (Chile), the Observatorio del Roque de los Muchachos, La Palma (Spain), CTIO (Chile) and SAAO (Sutherland).

REFERENCES

Antonucci R. R. J., Cohen R. D., 1983, ApJ, 271, 564
Avni Y., 1976, ApJ, 210, 642
Barr P., Mushotzky R. F., 1986, Nat, 320, 421
Barr P., Clavel J., Giommi P., Mushotzky R. F., Madejski G., 1987, in Treves A., ed., Variability of Galactic and Extragalactic X-ray Sources. Associazione per l'Avanzamento dell'Astronomia, Milan–Bologna, p. 43
Barylak M., Watasonic R., Imhoff C., 1985, ESA IUE Newsl., 20, 55
Bell Burnell S. J., Chiappetti L., 1984, A&AS, 56, 415
Boggess A. et al., 1978a, Nat, 275, 372
Boggess A. et al., 1978b, Nat, 275, 377
Bohlin R. C., Grillmair C., 1988, ApJS, 66, 209
Bohlin R. C., Savage B. D., Drake F. J., 1978, ApJ, 224, 132
Bohlin R. C., Holm A. V., Lindler D. J., 1981, ESA IUE Newsl., 10, 10
Boroson T., 1981, ApJ, 46, 177
Brindle C., Hough J. H., Bailey J. A., Axon D. J., Ward M. J., Sparks W. B., McLean I. S., 1990, MNRAS, 244, 577
Byard P. L., Foltz C. B., Jenkner H., Peterson B. M., 1981, PASP, 93, 147
Carter B. S., 1990, MNRAS, 242, 1
Clavel J., 1983, MNRAS, 204, 189
Clavel J., Joly M., Collin-Souffrin S., Bergeron J., Penston M. V., 1983, MNRAS, 202, 85
Clavel J., Gilmozzi R., Prieto A., 1988, A&A, 191, 393
Clavel J. et al., 1991, ApJ, 336, 64
Clavel J., Nandra K., Makino F., Pounds K., Reichert G. A., Urry C. M., Wamsteker W., Peracaula-Bosch M., 1992, ApJ, 393, 113
Crenshaw D. M., Peterson B. M., 1985, ApJ, 291, 677
Dahari O., De Robertis M. M., 1988, ApJS, 67, 249
de Jong T., Clegg P. E., Soifer B. T., Rowan-Robinson M., Habing H. J., Houck J. R., Aumann H. H., Raimond E., 1984, ApJ, 278, L67
De Korte P. A. J., Bleeker J. A. M., den Boggende A. J. F., Branduardi-Raymont G., Brinkmann A. C., Culhane J. L., Gronenschild E. H. B. M., Mason I., McKechnie S. P., 1981, Space Sci. Rev., 30, 495
Devereux N., 1987, ApJ, 323, 91
Dower R. G., Griffiths R. E., Bradt H. V., Doxsey R. E., Johnston M. D., 1980, ApJ, 235, 355
Edelson R.A., Malkan M. A., 1986, ApJ, 308, 59
Elvis M., Lockman F. J., Wilkes B. J., 1989, AJ, 97, 777
Forman W., Jones C., Cominsky L., Julien P., Murray S., Peters G., Tananbaum H., Giacconi R., 1978, ApJS, 38, 357
Freeman K. C., 1970, ApJ, 160, 811
Glass I. S., 1984, MNRAS, 211, 461
Glass I. S., 1992, MNRAS, 256, 23P
Glass I. S., Moorwood A. F. M., 1985, MNRAS, 214, 429
Grosbøl P. J., 1985, A&AS, 60, 261
Hamuy M., Maza J., 1987, A&AS, 68, 383
IRAS Point Source Catalog, 1985, Joint *IRAS* Science Working Group. Govt Printing Office, Washington, DC
Isobe T., Feigelson E. D., Akritas M. J., Babu G. J., 1990, ApJ, 314, 104
Kent S. M., 1985, ApJS, 59, 115
Kollatschny W., Fricke K. J., 1985, A&A, 143, 393
Koski A. T., Osterbrock D. E., 1976, ApJ, 203, L49
Kotilainen J. K., Ward M. J., Boisson C., DePuy D. L., Bryant L. R., Smith M. G., 1992, MNRAS, 256, 125
Kotilainen J. K., Ward M. J., Williger G. M., 1993, MNRAS, 263, 655
Kwan J., Krolik J. H., 1981, ApJ, 250, 478
Lawrence A., Rowan-Robinson M., Efstathiou A., Ward M. J., Elvis M., Smith M. G., Duncan W. D., Robson E. I., 1991, MNRAS, 248, 91
Lewis D. W., McAlpine G. M., Koski A. T., 1978, BAAS, 10, 388
Lynden-Bell D., 1969, Nat, 223, 690
McAlary C. W., Rieke G. H., 1988, ApJ, 333, 1
McAlary C. W., McLaren R. A., McGonegal R. J., Maza J., 1983, ApJS, 52, 341
McAlpine G. M., Williams G. A., Lewis D. W., 1979, PASP, 91, 746
MacKenty J. W., 1990, ApJS, 72, 231
Maoz D., Netzer H., Peterson B. M. et al., 1993, ApJ, 404, 576
Marshall F. E., Boldt E. A., Holt S. S., Mushotzky R. F., Pravdo S. H., Rothschild R. E., Serlemitsos P. J., 1979, ApJS, 40, 657
Martin P. G., Thompson I. B., Masa J., Angel J. R. P., 1983, ApJ, 266, 470
Morris S. L., Ward M. J., 1988, MNRAS, 230, 639
Parmar A. N., Izzo C., 1986, The EXOSAT Express, 16, 21
Peterson B. M., 1987, ApJ, 312, 79
Peterson B. M., Crenshaw D. M., Meyers K. A., 1985, ApJ, 298, 283
Reichert G. A., Mushotzky R. F., Petre R., Holt S. S., 1985, ApJ, 296, 69
Reichert G. A. et al., 1994, ApJ, 425, 582
Sanders D. B. et al., 1989, ApJ, 347, 29
Santos-Lleó M., Clavel J., Barr P., Glass I. S., Pelat D., Peterson B. M., Reichert G., 1994, MNRAS, in press (Paper 2)
Seaton M. J., 1979, MNRAS, 187, 73P
Sonneborn G., Garhart M. P., 1986, NASA IEU Newsl., 31, 29
Turner M. J. L., Smith A., Zimmermann H. U., 1981, Space Sci. Rev., 30, 513
Turner T. J., Pounds K. A., 1989, MNRAS, 240, 833
Ulvestad J. S., Wilson A. S., 1984, ApJ, 285, 439
Wamsteker W., Rodríguez P. M., Wills B. J., Netzer H., Wills D., Gilmozzi R., Barylak M., Talavera A., Maoz D., Barr P., Heck A., 1990, ApJ, 354, 446
Ward M., Elvis M., Fabbiano G., Carleton N. P., Willner S. P., 1987, ApJ, 315, 74
Wills B. J., Netzer H., Wills D., 1985, ApJ, 288, 94
Yee H. K. C., 1983, ApJ, 272, 473

APPENDIX A: LINE PROFILE ANALYSIS

In this appendix we describe the line profile decomposition method. Two techniques have been used. The first method is a straight summation of the flux in two independent velocity bins, the 'core' and the 'red wing'. The second method uses a multi-Gaussian decomposition technique.

The intensity of the 'core' is defined as the sum of the flux above the continuum integrated over the velocity range 0–1500 km s^{-1}. The 'red wing' intensity represents the integral of the line flux at velocities larger than +3000 km s^{-1}. A gap of 1500 km s^{-1} is left to minimize the possible contamination of one component by the other. In the case of the C IV λ1549 line, the blue wing ($v \leq -3000$ km s^{-1}) can also be measured. The results are listed in Table A1.

The C IV λ1549 is the best measured line and the only one whose profile warrants a Gaussian decomposition. The most successful model, which is able to reproduce the observed profile at all epochs with the minimum number of free parameters, involves five components: one each for the adjacent N IV] λ1486 and He II λ1640 features and three for the C IV line itself. These C IV components are (i) the blue shoulder whose centroid is shifted by −4900 km s^{-1} with respect to the systemic velocity and accounts for a blueward asymmetry of the C IV λ1549 profile; (ii) the very broad component, centred at −400 km s^{-1}, and (iii) the core component, fixed at the systemic velocity. The average linewidths are listed in Table A2. The C III] λ1909 + Si III] λ1892 profile can be modelled only by averaging together all the SWP spectra. No more than two Gaussians of equal width and centred at the wavelengths expected for each line are required for this fit. The red half of the Ly α λ1216 profile, on the average SWP spectra, can be characterized by a core of FWHM = 3200 km s^{-1} plus at least two more components to account for the N V λ1240 line and a very broad Ly α λ1216 wing. After removal of the Fe II and Balmer continuum emission (Section 4), each Mg II λ2798 profile can be well accounted for with one Gaussian only, which has a mean FWHM of 3400 ± 400 (rms) km s^{-1}.

The decomposition of the Hα λ6563 profile involves five Gaussians, one each for the two components of the [N II] λλ6548, 6584 doublet and three for the Hα λ6563 line itself (a narrow, a broad and a red one of intermediate width). Five Gaussian components are necessary to fit the Hβ λ4861 spectral region: one for the He II λ4686 line, one for each of the 4959-Å and the 5007-Å components of the [O III] doublet and two (narrow plus broad) for Hβ λ4861 proper. Only two Gaussians are necessary to deblend the Hγ λ4340 and [O III] λ4363 lines.

Linewidths are listed in Table A2. The errors have been estimated from the rms deviations combined with the propagation of the uncertainty on the adjacent continuum. It is worth pointing out that the FWHMs of the C III], Si III] and Mg II lines are the same, within the uncertainty, as that of the C IV core component. None of them shows the very extended wings which characterize the C IV λ1549 feature.

Table A1. Lyα and C IV line profile decomposition.

JD	Lyα$_{CORE}$ 1226-1232 Å	Lyα$_{RED}$ 1238-1264 Å	CIV$_{CORE}$ 1562-1570 Å	CIV$_{RED}$ 1578-1610 Å
4085.5	69±3	75±7	51±3	25±6
4388.5	49±3	39±7	49±3	13±6
4636.0	38±3	35±7	40±3	14±6
4731.7	55±3	70±7	47±3	29±6
4740.5	39±3	42±7	40±3	18±6
5502.6	43±3	49±7	37±3	18±6
5732.9	52±3	65±7	47±3	25±6
5735.8	45±3	46±7	44±3	25±6
6107.9	53±3	50±7	53±3	23±6
6111.8	44±3	40±7	50±3	26±6
6115.9	45±3	57±7	46±3	20±6
6119.7	56±3	58±7	58±3	28±6
6123.8	33±3	30±7	41±3	18±6
6241.4	30±3	32±7	31±3	15±6
6246.5	28±3	27±7	30±3	19±6
6251.4	28±3	30±7	25±3	12±6
6440.8	67±3	66±7	58±3	49±6
6972.4	55±1	74±3	59±1	29±3
7140.1	51±3	52±7	52±3	34±6
7143.9	66±1	81±3	57±1	34±3

Intensities in units of 10^{-14} erg s^{-1}cm^{-2} and corrected for reddening [$E(B-V) = 0.029$].

Table A2. Mean emission linewidths.

Line	FWHM km s^{-1}
Lyαλ1216[a]	3200±400
N IV]λ1486	3000±1000
C IVλ1549 total	4100±400
C IVλ1549 Blue	2100
C IVλ1549 Core	3100
C IVλ1549 Very broad	9700
He IIλ1640	7100±2400
Si III]λ1892	2910
C III]λ1909	2910
Mg IIλ2798	3400±600
He IIλ4686	8000±2400
HβBroad	4400±330
HeIλ5875 Broad	5500±1200
Hα Broad	4100±400
Hα Red	1000±500

[a] Very broad wing with a red half similar to the very broad C IV component.